Chapter 22
Simulation of Fundamental Properties of CNT- and GNR-Metal Interconnects for Development of New Nanosensor Systems

Yuri N. Shunin, Yu.F. Zhukovskii, N.Yu. Burlutskaya, V.I. Gopeyenko, and S. Bellucci

Abstract Cluster approach based on the multiple scattering theory formalism, realistic analytical and coherent potentials, as well as effective medium approximation (EMA-CPA), can be effectively used for nano-sized systems modeling. Major attention is paid now to applications of carbon nanotubes (CNTs) and graphene nanoribbons (GNRs) with various morphology which possess unique physical properties in nanoelectronics, *e.g.*, contacts of CNTs or (GNRs) with other conducting elements of a nanocircuit, which can be promising candidates for interconnects in high-speed electronics. The main problems solving for resistance C-Me junctions with metal particles appear due to the influence of chirality effects in the interconnects of single-wall (SW) and multi-wall (MW) CNTs, single-layer (SL) and multi-layer (ML) GNRs with the fitting metals (Me = Ni, Cu, Ag, Pd, Pt, Au) for the predefined carbon system geometry. Using the models of '*liquid metal*' and '*effective bonds*' developed in the framework of the presented approach and Landauer theory, we can predict resistivity properties for the considered interconnects. We have also developed the model of the inter-wall interaction inside MW CNTs, which demonstrates possible 'radial current' losses. CNT- and GNR- Metal interconnects in FET-type nanodevices provide nanosensing possibilities for local physical (mechanical), chemical and biochemical influences of external medium. At the same time, due to high

Y.N. Shunin (✉) • N.Yu. Burlutskaya • V.I. Gopeyenko
Information Systems Management Institute, 91 Ludzas, LV-1019 Riga, Latvia
e-mail: shunin@isma.lv; Natalja.burlucka@isma.lv; viktors.gopejenko@isma.lv

Yu.F. Zhukovskii
Institute of Solid State Physics, University of Latvia, 8 Kengaraga str., LV-1063 Riga, Latvia
e-mail: quantzh@latnet.lv

S. Bellucci
INFN-Laboratori Nazionali di Frascati, Via Enrico Fermi, 40, 00044 Frascati (Rome), Italy
e-mail: bellucci@lnf.infn.it

concentrations of dangling bonds CNT- and GNR- Metal interconnects as interfaces are also considered as electrically, magnetically and chemically sensitive elements for novel nanosensor devices.

Keywords Carbon Nanotubes (CNT) • Graphene Nanoribbons (GNR) • Scattering theory • Electronic structure calculations • Resistance of CNT- and GNR-Me interconnects • Nanosensors

22.1 Introduction

In order to overcome disadvantages of nowadays microtechnology, the miniaturization of electronic devices, the integration level expansion and the increase of the operation frequencies and power density are required, including the use of adequate materials and innovative chip interconnects. Due to their unique physical properties, especially due to a ballistic mechanism of conductivity, carbon nanotubes (CNTs) attract a permanently growing technological interest, for example, as promising candidates for nanointerconnects in high-speed electronics [1]. New possibilities for modern nanolectronics are open with novel 'marginal' forms of graphene – nanoflakes (GNFs) and nanoribbons (GNRs), which in analogy with CNTs demonstrate a wasteless ballistic mechanism of conductivity. Graphene nanointerconnects are also important for nanotechnology. Full integration of graphene into conventional device circuitry would require a reproducible large scale graphene synthesis that is compatible with conventional thin film technology.

The main aim of the current study is the implementation of advanced simulation models for a proper description of the electrical resistance for *end* contacts between CNTs and GNRs of different morphologies and metallic substrates of different nature. An adequate description of nanotube chirality [2] is one of the key points for the proper simulations on electric properties of CNT-based nanoelectronic devices.

The resistance of contact between arbitrary CNT and metallic catalytic substrate can considerably exceed that observed separately in a nanotube and a metal [3]. The conductance between real metals and CNTs still occurs, but it is mainly due to the scattering processes, which are estimated to be rather weak [4].

The attention of the present research focuses basically on the junctions of carbon nanotubes (CNTs) and graphene nanoribbons (GNR) with contacting metallic elements of a nanocircuit. Numerical simulations on the conductance and resistance of these contacts have been performed using the multiple scattering theory and the effective media cluster approach. We have simulated both single-wall (SW) and multi-wall (MW) CNTs as well as single-layered (SL) and multi-layered (ML) GNRs with different morphology. Figure 22.1 represent the contacts of metal substrates with CNTs and GNRs, respectively, as prototype nanodevices. This is the main subject of our current research and modeling. The contact regions (CNT-Me and GNR-Me) are the objects of a microscopic approach responsible for the main contribution to the resistance. Meanwhile, the resistances of nanotubes, nanoribbons and the metallic substrate *per se* may be considered as macroscopic parameters.
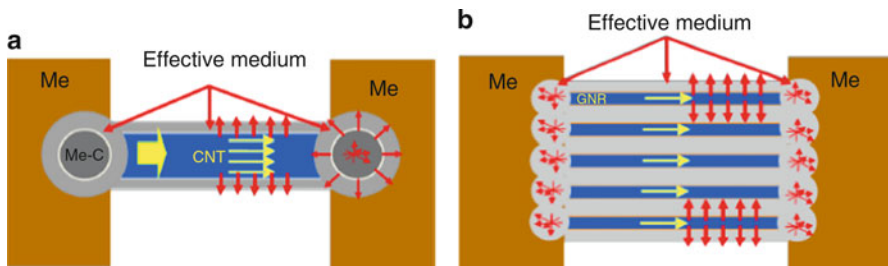
Fig. 22.1 Models of C-Me interconnects as a prototypes of novel nanodevices: (**a**) CNT-Me interconnect; (**b**) multilayered GNR-Me interconnect

22.2 Novel Nanodevices Models

22.2.1 CNT- and GNR-Based Sensors

There are some important applications of CNTs and GNRs based interfaces with other materials for novel nanosensor devices. Usually, these devices are considered as integrated devices around 10–50 μm^2 in size. The fundamental electron devices are FET-transistors (see Fig. 22.2a), which are very sensitive to various external influences of different nature such as mechanical, chemical, electrical, magnetic etc.

A field-effect transistor (FET) is nano in size, whose on/off threshold depends on the tube dimensions, shape and temperature, amongst others. A local deformation of CNT (GNR) creates a change in the on/off threshold voltage of the transistor. The electrical properties of carbon based interconnects are changes under the influence of external factors. The advantage of CNTs and GNRs over other materials occurs due to their small size, great strength, high electrical and thermal conductivity, and high specific area. Unique physical properties of CNTs and GNRs and their various interconnects allow considering them as sensing nanomaterials in various kinds of sensors – pressure, flow, thermal, gas, optical, mass, position, stress, strain, chemical, and biological sensors.

Taking into account specific physical properties of CNTs and GNRs metal interconnects, which are explained by the presence of 'dangling' chemical bonds, we should point out the expressed sensitivity of electric properties of interconnect space to chemical, electric and magnetic factors' influence. Therefore, we consider interconnects as a perspective group of nanosensors [5].

Based on **ab-initio** quantum transport calculations, molecular-dynamics simulation and continuum mechanics analysis [6] it has been proved that hydrostatic pressure can induce radial deformation and, consequently, electrical transition of SWNTs. A pressure-induced metal-to-semiconductor transition in armchair SWNTs has been observed, which provides a basis for designing nanoscale tunable pressure sensors.
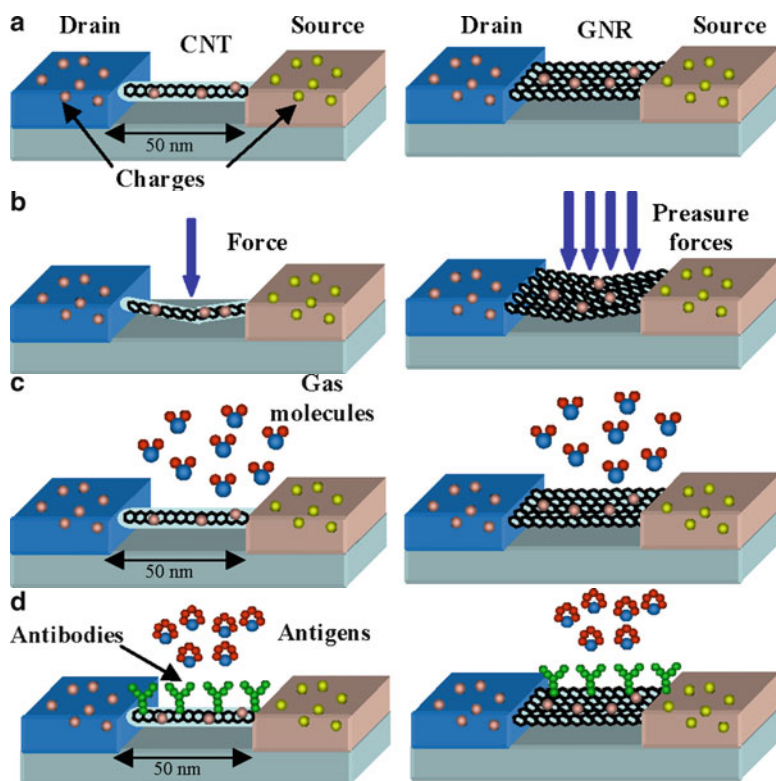
Fig. 22.2 (**a**) The unperturbed field-effect transistors based on a CNT and GNR are given CNT- or GNR- based FET is mainly composed of a corresponding semiconducting carbon material suspended over two electrodes. (**b**) *Physical nanosensors*: a conducting threshold can be altered when the tube or graphene ribbon is bent. (**c**) *Chemical nanosensors:* This threshold can be altered when the amount of free charges on the tube of graphene ribbon surface is increased or decreased by the presence of donor or acceptor molecules of specific gases or composites. (**d**) *Biological nanosensors:* monitoring of biomolecular processes such as antibody/antigen interactions, DNA interactions, enzymatic interactions or cellular communication processes, amongst others

Amperometric biosensors on the basis of CNTs immobilization matrix have been prposed in [7]; MWCNTs have been grown on a platinum (Pt) substrate. The MWCNT-Pt interconnect provides the signal monitoring of glucose (gluconic acid) concentration on the opposite side of MWCNTs array. Flow sensors based on SWNT bundles with CNTs producing electrical signal in response to fluid flow directly have also been developed [8].

The recent classification of nanosensors based on CNTs and GNRs considers three main groups: physical, chemical and biological [9].

Physical nanosensors are used to measure magnitudes such as mass, pressure, force, or displacement. The working principle is usually based on the fact that the electronic properties of both nanotubes and nanoribbons change when these are bent or deformed [10].

For example, a CNT can be used to build a field-effect transistor (FET) nano in size, whose on/off threshold depends on the tube dimensions, shape and temperature, amongst others. A local deformation of the tube/ribbon creates a change in the on/off threshold voltage of the transistor (Fig. 22.2b).

Starting from this simple principle, different types of nano-electromechanical systems (NEMSs) have been proposed in the literature with different applications, such as pressure nanosensors [11], force nanosensors [12] or displacement nanosensors [13].

Chemical nanosensors are used to measure magnitudes such as the concentration of a particular gas, the presence of a specific type of molecules, or the molecular composition of a substance. The functioning of the most common type of chemical nanosensors is based on the fact that the electronic properties of CNTs and GNRs change when different types of molecules are adsorbed on their top, which locally increases or decreases the number of electrons able to move through the carbon lattice (Fig. 22.2c).

Similarly to physical sensors, the presence of a specific type of molecules changes the on/off threshold voltage of the transistor when a nanotube or a nanoribbon is used in a transistor configuration [14].

Biological nanosensors are used to monitor biomolecular processes such as antibody/antigen interactions, DNA interactions, enzymatic interactions or cellular communication processes, amongst others (Fig. 22.2d). A biological nanosensor is usually composed of (i) a biological recognition system or bioreceptor, such as an antibody, an enzyme, a protein or a DNA strain, and (ii) a transduction mechanism, e.g., an electrochemical detector, an optical transducer, or an amperometric, voltaic or magnetic detector [15].

Electrochemical biological sensors work in a similar way as chemical nanosensors, but in this case, the change might be in the electronic properties of a protein, for example, or of any other chemical composite that binds itself to the functionalized nanotube. A specific antigen that binds itself to an antibody stuck to the nanotube. A single stranded DNA chain binds itself to another DNA chain which has been attached to the nanotube [16]. There are commercial nanosensors based on this principle. They are able to detect lung cancer, asthma attacks, different common viruses such as the influenza virus, or the parasites responsible for malaria [17].

The second subtype of biological nanosensors is based on the use of noble metal nanoparticles and the excitation using optical waves of surface plasmons, i.e., coherent electron waves at the interfaces between these particles. Simply stated, the resonant frequency of the surface plasmons, resulting from light irradiation, changes when different materials are adsorbed on and in between the particles. This technique, known as localized surface plasmon resonance (LPSR), is the underlying principle behind many biological nanosensors [18].

One of the main constraints of this sensing mechanism is the requirement of an external source of light and a device which is able to measure and compare different resonant frequencies of the particles. For example, nanosensors could locally irradiate the same particles with a much lower power and measure the reradiated energy at different frequencies.

There are various classes of CNT- and GNR-based nanosensors. A wide class of bionanosensors are used in the ***biomedical industry***, e.g., in such cases as diabetes, where regular tests by patients themselves are required to measure and control the sugar level in the body. Pressure nanosensors find application in many diagnostic and therapeutic devices. They can be used in eye surgery, hospital beds, respiratory devices, patient monitors, inhalers, and kidney dialysis machines, in both invasive and noninvasive blood pressure monitoring [19].

Nanosensors have a substantial utility in the automotive industry and their importance is expected to increase while designing the vehicles of the future [20]. In particular, they are used to process information about vehicle parameters such as pressure, vehicle altitudes, flow, temperature, heat, humidity, speed and acceleration, exhaust gas, and engine knock and torque.

Nanobiosensors are widely used in ***food industry*** to provide safety and quality control of food products as the contamination of foods caused by bacterial pathogens may result in numerous diseases [21].

Gas nanosensors can improve real-time ***environmental monitoring*** of combustible gas alarms, gas leak detection/alarms, biowarfare (e.g., monitoring explosives such as TNT or RDX and nerve agents such as GB or VX), environmental pollution monitoring, and cooking controls, etc. Unlike conventional solid-state gas sensors [22], which require relatively high temperatures to achieve significant sensitivity for gas molecules, CNT-based miniaturized gas sensors can work at room temperature.

There is another significant area of biosensors application besides medical and domestic purposes. Humidity bionanosensors are used to monitor humidity in green houses in ***agriculture and fishing industry***. Humidity and temperature conditions have a direct impact on the quantity and quality of the product [23].

Hydrogen gas nanosensors are used in ***manufacturing industry*** for hydrogen monitoring and control for petroleum transformation, welding, rocket engines, and fuel cells [24].

High sensitivity and low power consumption make nanosensors suitable, especially, for high accuracy and battery-powered applications, e.g., for ***military purposes***. Since purified CNTs have very large surface area ($1.587 \text{ m}^2/\text{g}$) [25] and extremely high conductivity, CNT composites show low threshold and sharp slope of percolation conductivity around the threshold. Nanosensors using CNT composites as sensing materials have higher sensitivity. CNT-based sensors are potentially applied in defense and homeland ***security*** [26].

22.2.2 *Nanodevices for Effective Electron Transport*

The electronic structure for CNT-Me and GNR-Me interconnects can be evaluated through the electronic density of states (DOS) for carbon-metal contact considered as a 'disordered alloy', where clusters containing both C and Me atoms behave as scattering centers. The computational procedure that we have developed for these
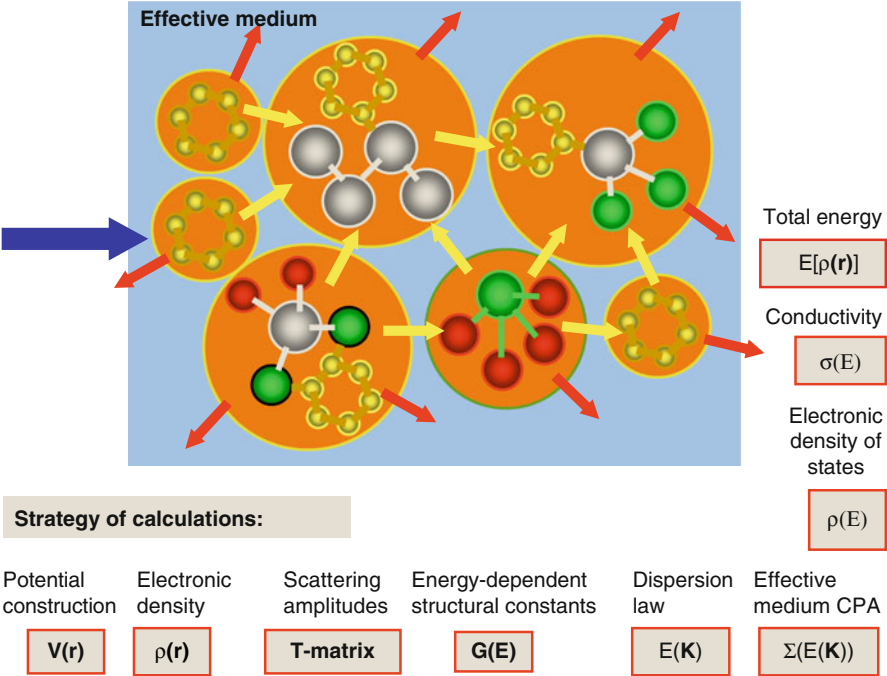
Fig. 22.3 Multiple scattering problem for the system of clusters as multiple scattering model of condensed matter: strategy of calculations on fundamental properties of condensed medium described within the effective media approximation

calculations [27] is based on the construction of cluster potentials and the evaluation of both scattering (S) and transfer (T) matrices. The general model of multiple scattering using the effective media approximation (EMA) combined with the coherent potential approach (CPA) for condensed matter is based on the atomic cluster formalism. When using the CPA as EMA approximation, the resistance of the interconnect is evaluated through Kubo-Greenwood formalism [5, 28] or, in the simplest cases, through Ziman model [29].

The general model of multiple scattering with effective media approximation (EMA) for condensed matter based on the approach of atomic cluster is presented in Fig. 22.3. So far, the cluster formalism has been successfully applied for metal Cu metal [27], as well as for semiconductors, both elemental (Ge and Si) and binary (As_xSe_{1-x} and Sb_xSe_{1-x}) [30]. Special attention has been paid for the latter, since the concept of statistical weighing has been applied for the binary components in solid solutions.

We have developed structural models for CNT-Me and GNR-Me junctions, based on their precise atomistic structures, which take into account the CNT chirality effect and its influence on the interconnect resistance for Me (= Ni, Cu, Ag, Pd, Pt, Au) and pre-defined CNT (or GNR) geometry.

In the simplest cases, the electronic structure for the CNT-Ni interconnects, can be evaluated through the DOS for the C-Ni contact considered as a 'disordered alloy' [28]. In the current study, we have developed more complicated structural models of CNT-metal junctions based on a precise description of their atomistic structures. When estimating the resistance of a junction between a nanotube and a substrate, the main problem has been caused by the influence of the nanotube chirality on the resistance of SW and MW CNT-Me interconnects (Me = Ni, Cu, Ag, Pd, Pt, Au), for a pre-defined CNT geometry.

22.3 Multiple Scattering Theory and Effective Medium Approach for CNT GNR Interconnects' Simulation

The resistivity can be considered as a scattering problem, where the current carriers participate in the transport, according to various mechanisms based on the presence of scattering centers (phonons, charge defects, structural defects, *etc.*), including a pure elastic way, called ballistic. The developed computational procedure [27, 30] is based on the construction of cluster potentials and the evaluation of the S- and T-matrices for scattering and transfer, respectively. It allows us to realize the full-scale electronic structure calculations for condensed matter ('black box'), where ***influence*** means a set of electronic 'trial' energy-dependent wave functions $\Psi_{in}(\mathbf{r})$ and ***response*** $\Psi_{out}(\mathbf{r})$ gives sets of scattering amplitudes corresponding to possible scattering channels for any 'trial' energy. This allows us 'to decrypt' the electronic spectra of 'black box' [5, 30].

We consider a domain where the stationary solutions of the Schrödinger equation are known, and we label them as

$$\psi_{in}(\mathbf{r}) = \phi_{\mathbf{k}}(\mathbf{r}) = \exp(i\mathbf{k}\mathbf{r}). \tag{22.1}$$

The scattering of 'trial' waves, in the presence of a potential, yields new stationary solutions labeled as

$$\psi_{out}(\mathbf{r}) = \psi_{\mathbf{k}}^{(\pm)}(\mathbf{r}) \tag{22.2}$$

for the modified Schrödinger equation $\hat{H}\psi_{\mathbf{k}}^{(\pm)}(\mathbf{r}) = E\psi_{\mathbf{k}}^{(\pm)}(\mathbf{r})$. An electronic structure calculation is considered here as a scattering problem, where the centers of scattering are identified with the atoms of clusters [27].

The first step to modeling is the construction of potentials, both atomic and crystalline, which is based on analytical Gaspar's potential of screened atomic nucleus [31] and X_α and $X_{\alpha\beta}$ presentations for the electronic exchange and correlation, using the LDA (Local Density Approximation). Figure 22.4 shows both atomic and crystalline potentials for carbon as compared to the Hartree-Fock atomic potential. Then, we apply the so-called muffin-tin approximation (*MTA*) for potential models.
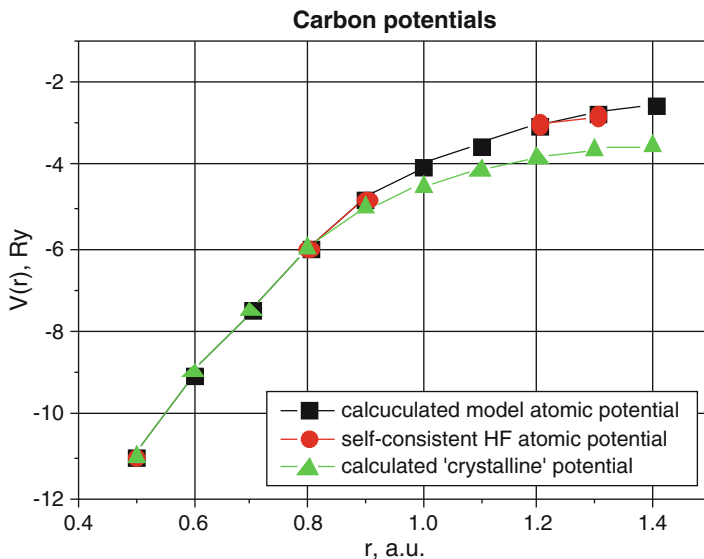
Fig. 22.4 Analytical carbon potentials based on simulation procedure as compared to the results of Hartree-Fock calculations

To obtain the electronic structure, the calculations on scattering properties are necessary, generally, in the form of *S*- and *T*-matrices (Fig. 22.3). These calculations start with the definition of the initial atomic structure to produce a medium for the solution of the scattering problem for a trial electronic wave [27]. The results of potential modeling and phase shifts in the framework of *MT*-approximation are presented elsewhere [27, 30].

The formalism used here for calculations on the electronic structure is based on the CPA [32], the multiple scattering theory [33] and cluster approach [34]. As a *first step*, we postulate the atomic structure at the level of short- and medium-range orders. As a *second step*, we construct a "crystalline" potential and introduce the muffin-tin (*MT*) approach. This is accomplished by using realistic analytical potential functions.

The scattering paradigm for the simplest cases of spherically symmetrical potentials (elastic scattering) looks as follows:

$$\psi(\mathbf{r}) \rightarrow e^{ikz} + f(\theta)\frac{e^{ikr}}{r} \text{ (``liquid metal'' model)} \tag{22.3}$$

and

$$\psi(\mathbf{r}) \rightarrow e^{ikz} + f(\theta, \varphi)\frac{e^{ikr}}{r} \text{ (spherical cluster model)} \tag{22.4}$$

Then, the electronic wave scattering problem is solved, and the energy dependence of the scattering properties for isolated *MT* scatterers is obtained in the form

of the phase shifts $\delta_{lm}(E)$, and the T-matrix of the cluster is found as a whole. The indices l and m arise, as a result of expansions of such functions as Bessel's functions j_l, Hankel's functions h_l and spherical harmonics Y_{lm}.

In general, the modeling of disordered materials represents them as a set of atoms or clusters immersed in an effective medium, with the dispersion $E(\mathbf{K})$ and a complex energy-dependent coherent potential $\Sigma(E)$ found self-consistently in the framework of the CPA. The basic equations of this approach are:

$$\Sigma(E) = V_{eff} + \langle T \rangle (1 + G_{eff} \langle T \rangle)^{-1}, \tag{22.5}$$

$$G(E) = G_{eff} + G_{eff} \langle T \rangle G_{eff} = \langle G \rangle, \tag{22.6}$$

$$\langle T(E, \mathbf{K}) \rangle = 0, \tag{22.7}$$

$$\Sigma(E) = V_{eff}, \tag{22.8}$$

$$\langle \mathrm{G} \rangle = G(E) = \mathrm{G}_{eff}, \tag{22.9}$$

$$N(E) = -(2/\pi) \ln \{ \det \| G(E) \| \} . \tag{22.10}$$

Here $<\ldots>$ denotes averaging, V_{eff} and G_{eff} are the potential and the Green's function of the effective medium, respectively, $T(E,\mathbf{K})$ the T matrix of the cluster, and $N(E)$ the integral density of the electronic states. Equation 22.7 can be rewritten in the form:

$$\langle T(E, \mathbf{K}) \rangle = \mathbf{Sp} T(E, \mathbf{K}) = \int_{\Omega_{\mathbf{K}}} \langle \mathbf{K} | T(E, \mathbf{K}) | \mathbf{K} \rangle d\Omega_{\mathbf{K}} = 0, \tag{22.11}$$

where $|\mathbf{K}\rangle = 4\pi \sum_{l,m} (\mathrm{i})^l j_l(kr) Y_{lm}^*(\mathbf{K}) Y_{lm}(\mathbf{r})$ is the one-electron wave function, $\mathbf{Sp}$ means the calculation of the matrix trace while the integration is performed over all angles of $\mathbf{K}$ inside the volume $\Omega_{\mathbf{K}}$. Equation 22.7 enables one to obtain the dispersion relation $E(\mathbf{K})$ of the effective medium. The DOS calculations have been performed using the relation:

$$\rho(E) = \frac{2}{\pi} \int \mathrm{Im}\{ \mathbf{Sp} G(\mathbf{r}, \mathbf{r}', E) \} \, d\mathbf{r}, \tag{22.12}$$

where $G(\mathbf{r}, \mathbf{r}', E) = \sum_{l,m} Y_{lm}(\mathbf{r}) Y_{lm}(\mathbf{r}') G_l(\mathbf{r}, \mathbf{r}')$ is the angular expansion of Green function.

The paradigm of the scattering theory and the developed strategy of simulation of CNTs electronic properties use the generalized scattering condition for the low-dimensional atomic structures of the condensed matter:

$$\psi_{\mathbf{k}}^{(\pm)}(\mathbf{r}) \underset{r \to \infty}{\propto} \phi_{\mathbf{k}}(\mathbf{r}) + f_{\mathbf{k}}^{(\pm)}(\Omega) \frac{\exp(\pm ikr)}{r^{\frac{d-1}{2}}}, \tag{22.13}$$

where Ω describes the integrated space in angular units while superscripts '+' and '−' label the asymptotic behavior in terms of d-dimensional waves:

$$\frac{\partial \sigma_{a \to b}}{\partial \Omega} = \frac{2\pi}{\hbar v} \left| \langle \phi_b | \hat{V} | \psi_a^+ \rangle \right|^2 \rho_d(E), \tag{22.14}$$

where d is the atomic structure dimension.

22.3.1 Calculations of Conductivity and Resistance

The calculations of conductivity are usually performed using Kubo-Greenwood formula [35]:

$$\sigma_E(\omega) = \frac{\pi \Omega}{4\omega} \int [f(E) - f(E + \hbar \omega)] |D_E|^2 \rho(E) \rho(E + \hbar \omega) dE, \tag{22.15}$$

where ω is a real frequency parameter of Fourier transform for the time-dependent functions, $f(E)$ is Fermi-Dirac distribution function, $D_{E,E'} = \int_\Omega \Psi_{E'}^* \nabla \Psi_E d\mathbf{r}$, where $\Psi_{E(\mathbf{K})} = A \, exp(i\mathbf{K}\mathbf{r})$ and $\mathbf{K}$ is the complex wave vector of the effective medium. The dispersion function $E(\mathbf{K})$ determines the properties of the wave function $\Psi_{E(\mathbf{K})}$ upon the isoenergy surface in $\mathbf{K}$-space.

For static conductivity ($\omega = 0$ and T = 0 K), Eq. 22.16 gives the Drude-like formula:

$$\sigma_{E(\mathbf{K})} = \frac{e^2 n^*}{m^*} \tau, \tag{22.16}$$

where n^* is the effective electron density with a relaxation time $\tau \approx l/v_h$, $l(T)$ is the free path while a heat velocity is $v_h = (3kT/m^*)^{1/2}$. The effective electron mass can be defined using the dispersion law:

$$m^* = (\partial^2 E / \partial K_R^2)^{-1}, \tag{22.17}$$

where K_R is a modulus of the real part of the vector $\mathbf{K}$.

There exist some ideas to estimate the conductivity in static and frequency regimes taking into account the temperature effects. However, in the case of CNT (of GNR), we must consider not only the diffusive mechanism of conductivity, but also the 'so-called' ballistic one. This is an evident complication in the interpretation of electrical properties of CNTs, GNRs and the related systems.

22.4 CNT- and GNR-Metal Interconnects Simulation Results

22.4.1 'Liquid Metal' Model for CNT-Metal Junction: CNT-NI Case

The term "liquid metal" means the structural disorder of the substance involved, more precisely, only the nearest order (short range order – SRO) is considered as it usually occurs in a liquid. It also means that the inter-atomic distance between the nearest neighbors (first coordination sphere) is fixed, whereas the angular coordinates are random. In the context of this model, the interconnect space C-Ni is considered as 'liquid' alloy C_xNi_{1-x}.

The model in CPA approach (22.11) gives the dispersion law for the effective medium and the electronic density of states (EDOS, see Eq. 22.12), where the argument $\mathbf{K}$ of dispersion function $E(\mathbf{K})$ is a complex: $\mathbf{K_R} + i\mathbf{K_I}$. The 'mixed' dispersion law [5, 27, 35]:

$$E_{C-Ni}(\mathbf{K_R}) = xE_C(\mathbf{K_R}) + (1-x)E_{Ni}(\mathbf{K_R}) \qquad (22.18)$$

means configurationally-averaged state of the electronic structure within the interconnect space with a variable extent of disorder. The 'liquid metal' alloy model can be used for evaluating mixed effective mass $m^*_{C-Ni}(E)$ (see Eq. 22.17). Taking into account the spectral dependence of the effective mass $m^*(E)$ and estimating the spectral resistivity $\rho_x(E)(1/\sigma_x(E))$, Eq. 22.16, we can estimate the average layer resistivity $\rho_{x,av}$ as:

$$\rho_{x,av} = \frac{\int\limits_{0}^{E_{fin}} \rho_x(E)dE}{E_{fin}}, \qquad (22.19)$$

where E_{fin} is the width of the conduction band and $x(z)$ is the stoichiometry coefficient depending on the coordinate z of the ring layer (Fig. 22.6). The evaluation of resistance for the CNT-Ni contact gives $\sim$105 kOhm for the nanotube with the internal and external radii – $R_1 = 1.0$ nm and $R_2 = 2.0$ nm, respectively. Evidently, the results of the resistance evaluation for interconnect depend essentially on both the layer height l_0 and the spectral integration parameter E_{fin}, which is responsible for the electron transport of really activated electrons.

The "liquid metal" model [5] does not operate with CNT chirality in the interconnect space. Limitations on chirality effect (e.g., chirality angle) in the CNT-Me junction forced us to develop a semi-empirical model that considers the local atomic structure of the interconnect. For this aim, we have constructed a model of 'effective bonds' for the interconnect with a realistic atomic structure.
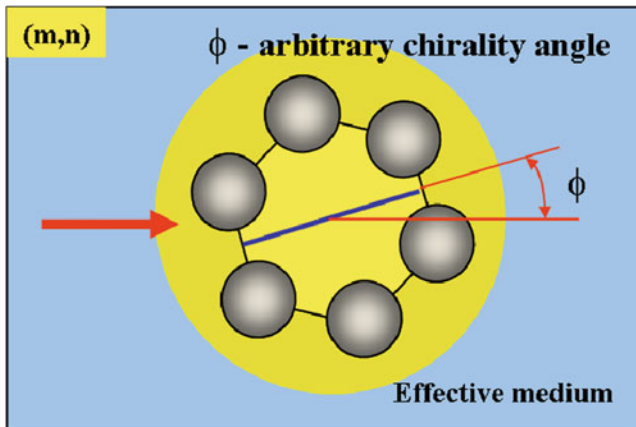
Fig. 22.5 Modeling of chirality: carbon ring rotation within CNT and GNR

22.4.2 Model of 'Effective Bonds' for Simulations of CNT-Me and GNR-Me Junctions

The model of CNT-Me and GNR-Me nanointerconnects (Fig. 22.1) has been developed in the current study. Within the electronic transport formalism, it consists of two regions supporting two different electron transport mechanisms: *ballistic* (elastic) and *collisional* (non-elastic). These electron transport processes are simulated using the corresponding boundary conditions in the form of the effective medium. The CNT and GNR chiralities (*m,n*) are simulated by the corresponding orientation of the chirality vectors within the scattering medium. The most problematic regions for simulation are Carbon-Me junctions, where atomic structural disorder is observed and the conductivity mechanism is changed. The chirality influence on the resistance in the region of interconnect depends on a number of statistically realized bonds between a carbon nanostructure and a metal contact (*e.g.*, Ni, Cu, Au, Ag, Pd, Pt).

Using the simulation models, presented earlier [1, 2] , we have determined the resistance for both (SW&MW) CNT-Me and (SL&ML) GNR-Me interconnects, based on the evaluation of the interface potential barriers and implementation of Landauer formula [36], which defines the integrated conductance:

$$I_G = \frac{2e^2}{h} \sum_{i=1}^{N} T_i = \left(\frac{1}{12.92(kOhm)} \right) \sum_{i=1}^{N} T_i = 0.0774 \sum_{i=1}^{N} T_i. \qquad (22.20)$$

The chirality (*m,n*) is simulated by the corresponding orientation of carbon rings within the scattering medium (Fig. 22.5).
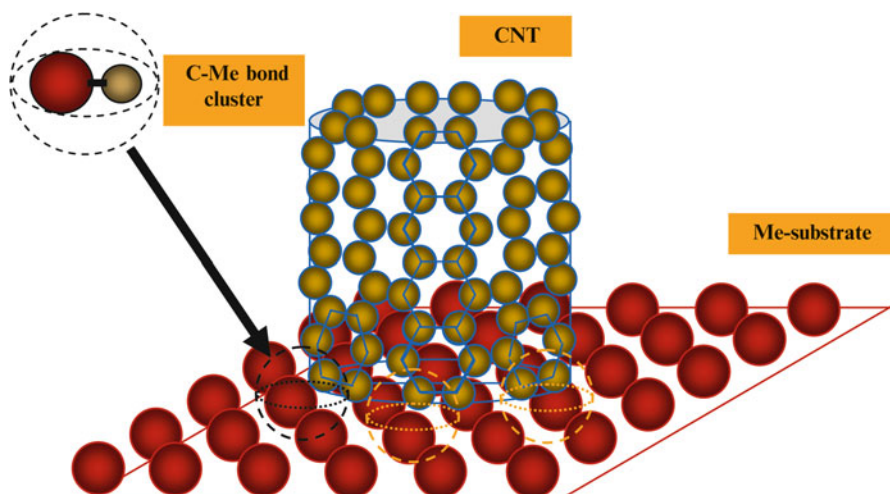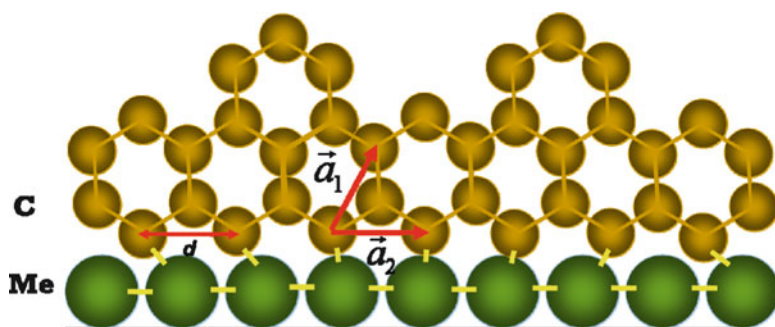
Fig. 22.6 CNT-Me interconnect formation model

Fig. 22.7 *Armchair* GNR-Me *end type* interconnect formation model

The most problematic areas for the proper simulation are CNT-Me and GNR-Me *end to* junctions (Figs. 22.6 and 22.7), where the atomic structural disorder is observed and the conductivity mechanism is changed.

The influence of chirality on resistance in the vicinity of interconnect depends on the number of statistically realized bonds between the CNT (GNR) and the metal contact (*e.g.*, Ni, Cu, Au, Ag, Pd, Pt).

In the case of *side type* contact for GNR-Me interconnects the number of effective bonds per contact square is essential (see Fig. 22.8).
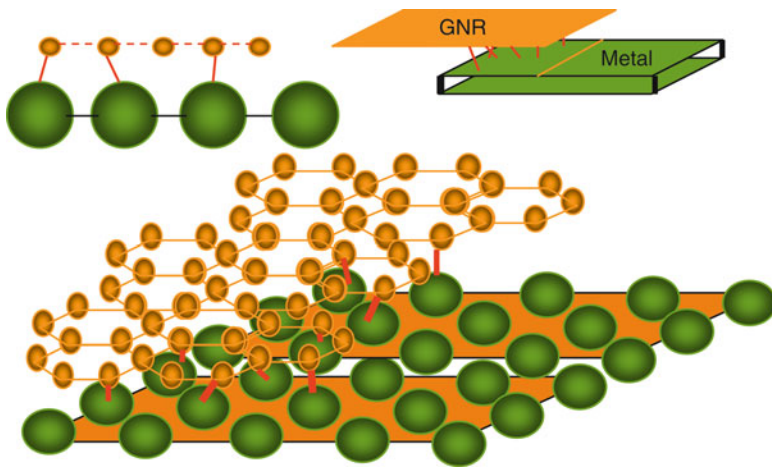
Fig. 22.8 GNR-Me *side type* interconnect formation model

22.4.3 SW CNTs, SL- and ML-GNRs Simulations

Figures 22.6 and 22.7 present a creation of C-Me 'effective bonds'. We consider here [001] substrates of *fcc*-metals. We should also underscore that this is a probabilistic process when only more-or-less equilibrium bonds ('effective bonds') are formed at inter-atomic distances corresponding to the minimum total energies. The evaluation of a number of "effective bonds" using Eq. 22.20 is principal for the number of 'conducting channels', since the conductance is proportional to the number of appeared "effective bonds" within the CNT-Me interconnect.

The calculations of conducting abilities of "effective bonds" lead us to estimate the energy-dependent transparency coefficient of a potential barrier C-Me (Figs. 22.9 and 22.10). The scattering process for this potential barrier is regulated by the effect of "thin film" for conductivity electrons, which leads to quantization in voltaic parameters (in the case of full transparency). The transmission (transparency) coefficient T for the barrier scattering problem (Fig. 22.10) is defined as:

$$T = \sqrt{\frac{E_2}{E_1}} \left(\frac{2\sqrt{E_1}}{\sqrt{E_1} + \sqrt{E_2}} \right)^2, \qquad (22.21)$$

where E_1 and E_2 are the corresponding electron energies. Evaluation of resistances of CNT-Ni junctions for various NT diameters and chiralities are presented in Table 22.1.

These resistances have been evaluated taking into account that only thermally activated electrons, *i.e.*, a small part Δn of all quasi-free electrons n, participates in
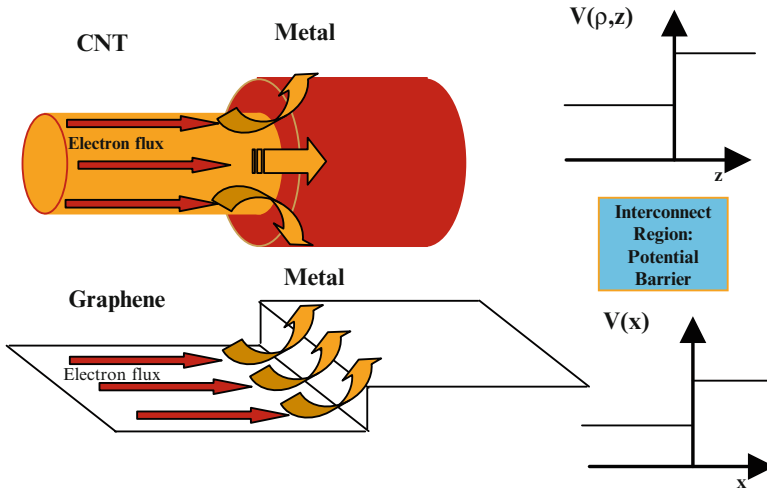
Fig. 22.9 Interconnect potential model for the scattering problem: CNT-Me, GNR-Me
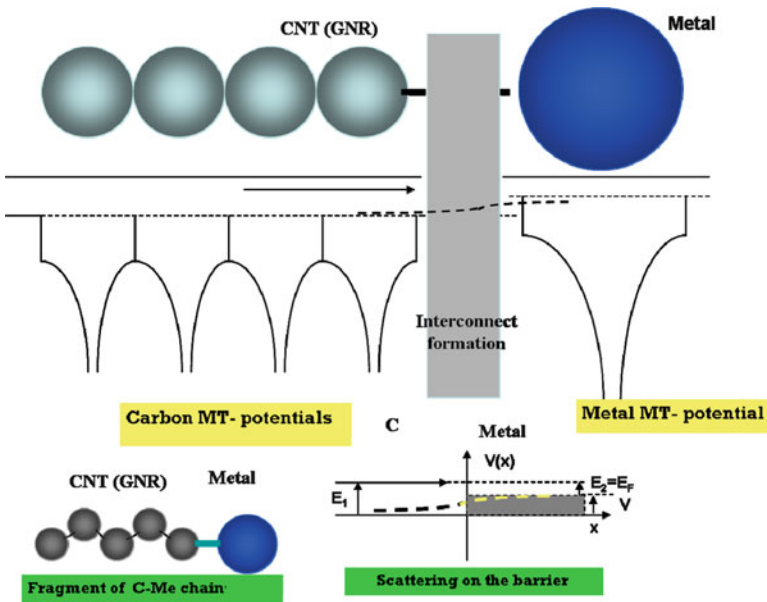
Fig. 22.10 Formation of a potential barrier for SW CNT-Me (SL GNR-Me) junction

the conduction process with Fermi velocity v_F. This ratio can be evaluated as follows:

$$\frac{\Delta n}{n} \approx \frac{\frac{1}{2}\rho(E_F(0)k\mathrm{T}}{\frac{2}{3}\rho(E_F(0))E_F(0)} = \frac{3}{4}\frac{k\mathrm{T}}{E_F(0)}, \tag{22.22}$$

Table 22.1 Resistances for the SW CNT-Ni interconnects

Diameter, nm	Chirality indices	Number of bonds in contact	Modulus of chirality vector, nm	Interconnect resistance, kOhm
Zig-zag, $\varphi = 0°$				
1.010	C(13,0)	12	2.952	665,19
2.036	C(26,0)	24	6.394	333,33
5.092	C(65,0)	64	15.990	124,72
10.100	C(130,0)	129	32.002	61,87
20.360	C(260,0)	259	63.940	30,82
Armchair, $\varphi = 30°$				
0.949	C(7,7)	12	2.982	665,19
2.035	C(15,15)	28	6.391	205,71
5.021	C(37,37)	72	15.765	111,11
10.041	C(74,74)	146	31.531	54,79
20.084	C(128,128)	294	63.062	27,21
C(3m,m), $\varphi = 14°$				
0.847	C(9,3)	3	2.66	2,666,66
1.694	C(18,6)	5	5.32	1,600,00
5.082	C(54,18)	16	15,96	500,00
10.16	C(108,36)	36	32.05	222,22
20.32	C(216,72)	80	64.10	100,00
C(2m,m), $\varphi = 19°$				
1.036	C(10,5)	5	3.254	1,600,00
2.072	C(20,10)	9	6.508	888,88
4.973	C(48,24)	17	15.614	470,50
10.1528	C(98,49)	47	31.880	170,21
20.5128	C(198,99)	97	64.410	82,47

See also Figs. 22.11 and 22.12

where $f(E)$ is Fermi-Dirac distribution function and $\rho(E)$ is a DOS while $kT = 0.0258eV$ for T $= 300°$ K.

The role of thermally activated electrons is described by the scattering mechanism changing in the space of CNT-Me interconnect. The mean free path L in the CNT is of order $10^2 - 10^4 \, a_C$, where a_C is a carbon covalent radius, which can be explained by the ballistic mechanism of electron transport within the energy channel of the CNT. At the vicinity of interconnect, we observe a drastic decrease of the electron mean free path down to 1–2 a_C. From the uncertainty condition $\kappa L \approx 1$ (where $L \sim a_C \sim 2 \, a.u.$ is a free path), we can evaluate Fermi electron wave number $\kappa \propto \kappa_F \approx 1/a_C \approx 0.5$ a.u.$^{-1}$. It means that $E_F \sim 0.25$ Ry, *i.e.*, a large increase of resistance occurs in the interconnect space. In particular, the variation of the chirality angle ϕ within the interconnect space leads to the fluctuation of the number of C-Me atomic bonds. In the case of $0° < \phi < 30°$, a certain number of non-stable and non-equilibrium bonds can be created. Evidently, this leads to the decrease of interconnect conductance, which is well-observed when performing variation of nanotube diameter (Fig. 22.11).
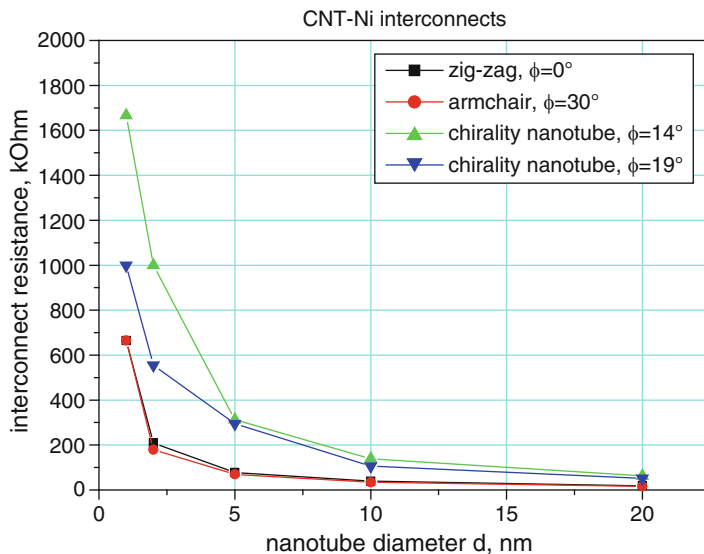
Fig. 22.11 CNT-Ni interconnect resistance *via* NT diameter

Specific results for chirality effect simulations are shown in Fig. 22.12, with the evident maximum of the resistance for $\phi \approx 15°$, where a large number of non-equilibrium bonds is formed, with higher potential barriers and lower transparency.

Figure 22.13 shows the generalized results of simulations on resistance of junctions obtained for various metallic substrates. It is clear that Ag and Au substrates are more effective electrically while Ni is rather a 'worse' substrate for interconnect, although it yields the most effective catalyst for CNT growth. On the other hand, the catalysts, which are usually used for the SW CNT growth (*e.g.*, Fe, Co and Ni), have stronger bonds to the ends of SW CNTs than noble metals [37], *i.e.*, some compromise exists between electrical parameters and strengths of the interconnect bonding.

Similar calculations have been carried out for special configuration of SL GNR-Me interconnect (Fig. 22.14) and for ML GNR-Me interconnect (Fig. 22.15).

22.4.4 Resistance MWCNT-Me Junctions

We have constructed atomistic models of both SW CNT bundles and MW CNTs which could fit into a porous alumina with diameters of holes ~20 nm. In particular, a model of MW CNT with a pre-defined combination of *armchair* (*ac*) and *zig-zag* (*zz*) shells is presented in Table 22.2.

Using the simulation models presented earlier, we have developed an "effective bonds" model for MWCNT-Me junction resistance [38], based on the interface
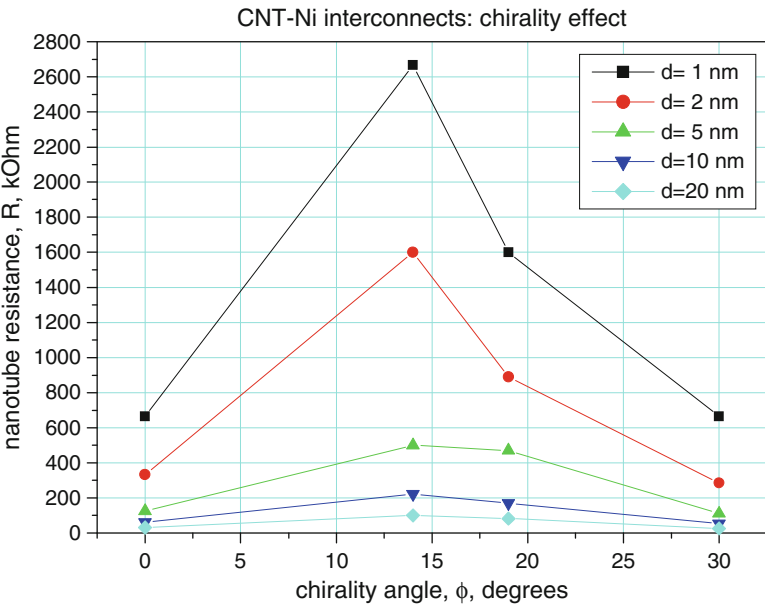
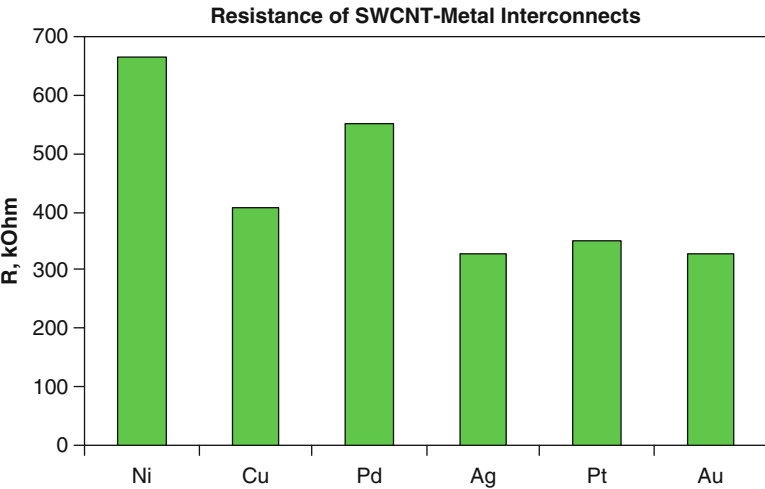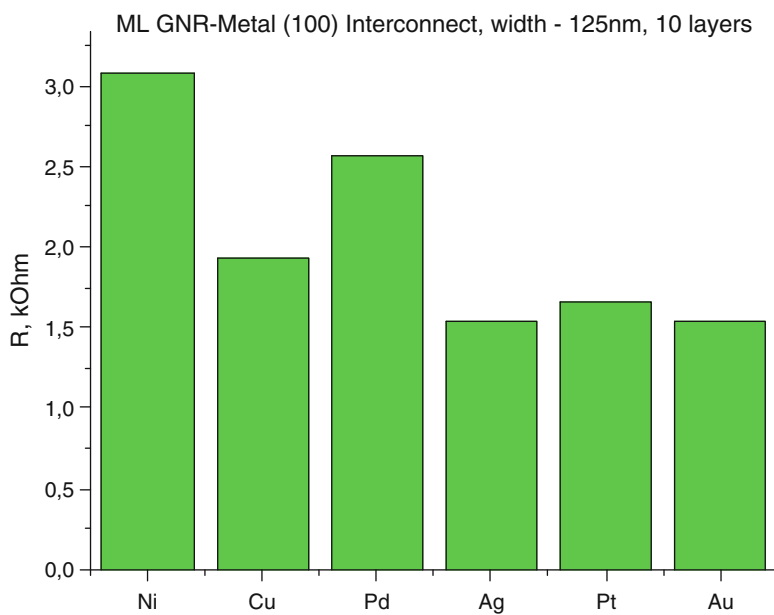**Fig. 22.12** CNT-Ni interconnect simulation: *chirality effects*

Fig. 22.13 Resistances of the zigzag-type SW CNT-Me interconnects for the CNT diameter ~1 nm

potential barriers evaluation and Landauer formula, Eq. 22.10. The results of these simulations are presented in Fig. 22.16. For MWCNT-Me junction, the integral bonding with a corresponding substrate may be not so significant as in the case of SW CNTs, where the weak bonding can be principal.

SL GNR-Metal (100) Interconnect, width - 125nm
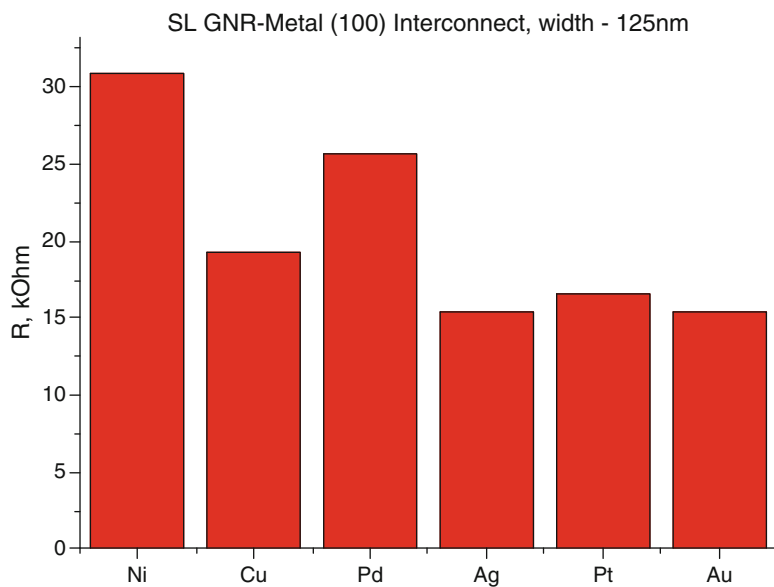
Fig. 22.14 Resistances of the SLGNR-Me interconnects

ML GNR-Metal (100) Interconnect, width - 125nm, 10 layers

Fig. 22.15 Resistances of the MLGNR-Me interconnects

Table 22.2 Details of the model for MW CNT-Me interconnect	Diameter of CNT shell, nm	Chirality
	12.88	(95,95) *ac*
	13.54	(173,0) *zz*
	14.24	(105,105) *ac*
	14.87	(190,0) *zz*
	15.58	(199,0) *zz*
	16.27	(120,120) *ac*
	16.99	(217,0) *zz*
	17.69	(226,0) *zz*
	18.44	(136,136) *ac*
	19.18	(245,0) *zz*
	19.88	(254,0) *zz*
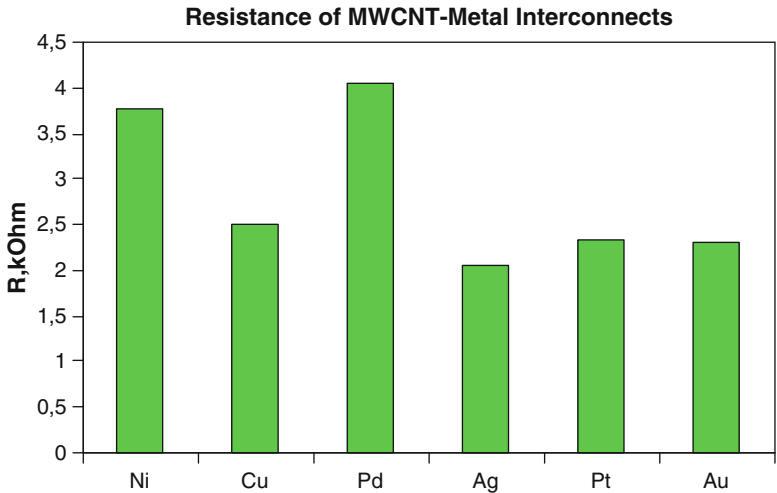
Fig. 22.16 Resistances of various MWCNT- Me interconnects

Figure 22.16 shows similar ratios of electric resistances as for SW CNTs (Fig. 22.13), in favor of Au, Ag and Pd.

22.4.5 Current Loss Between the Adjacent Shells Inside the MW CNT

Using the model of inter-shell potential within the MW CNT we have also evaluated the transparency coefficient, which determines the possible 'radial current losses. Figure 22.17 shows the inter-shell potential which is calculated using the developed realistic analytical potentials (see comments on the procedure of the potential construction, *e.g.*, in [27]).
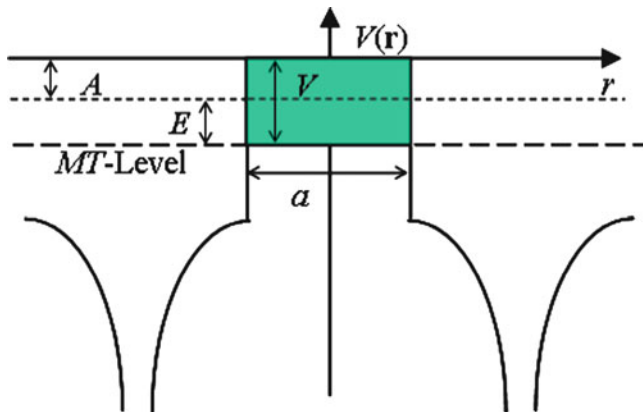
Fig. 22.17 Inter-shell transparency and inter-shell *MT*-potential model (*MT*-muffin tin)

In Fig. 22.17, A is the electron emission energy, E is the electron energy, V is the height of the potential barrier between the nearest atoms in neighboring nanotube shells. Thus, a radial transparency coefficient T for the two different energy ratios can be defined as:

$$E > V, T = \frac{4Ek_2^2}{(E - k_2^2)\sin^2 k_2 a + 4Ek_2^2}, \quad k_2^2 = E - V, \tag{22.23}$$

$$E < V, T = \frac{4E\kappa_2^2}{(E - \kappa_2^2)sh^2 \kappa_2 a + 4E\kappa_2^2}, \quad \kappa_2^2 = V - E, \tag{22.24}$$

where k_2 is the electron wave number in the case of above-barrier motion and κ_2 is the same for under-barrier motion. For example, between the 2nd and 1st shells (*zz-ac* case, Table 22.2) $a = 13.54 - 12.88 = 0.66$ nm $= 12.47$ a.u. and $T = 3.469 \cdot 10^{-6}$ *per* 1 bond.

Clearly, the total radial conductance is proportional to T and the number of effective potential barriers. It is also clear that the 'radial current' losses (or, simply radial current) are similar to the Hall current due to the induced magnetic field of the basic axial current. A pure scattering mechanism is also possible. However, the radial conductance *per* CNT length depends on the morphology (chirality) of the nearest nanotubes, when the number of shortest effective barriers is varied in a probabilistic way. This also means that current-voltage parameters of MW CNTs can be less stable, than in the case of SW CNTs. It has been found that inter-shell interactions, such as inter-shell tunneling of electrons and Coulomb interactions [39–41] cause a reduction of the total MW CNT conductance. This is also in agreement with evaluations in [45].
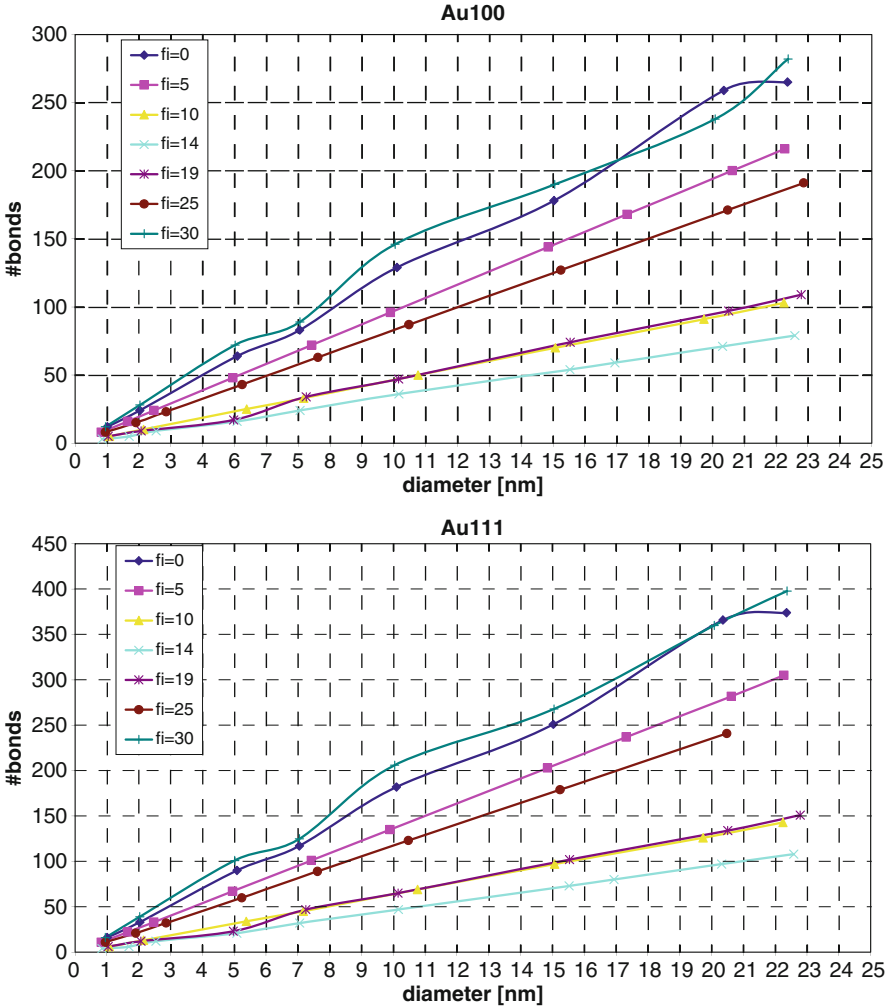
Fig. 22.18 Results of parametric calculations of resistances for Au-CNT interconnects

22.4.6 *Parametric Calculations of CNT-Me Interconnects Resistances*

We have also performed parametric calculations of resistances for Ni, Pd and Au CNT interconnects, where CNT diameter have been varied from 1 to 22 nm, and chirality angle from $0°$ to $30°$ (with the step $5°$) for the two basic metal substrate orientations ([100] and [111]). The aim of these detailed simulations is to create approximation dependences and data base of interconnect compositions for various technological applications [42, 43]. Technologically reasonable results of these simulations (Au-Me interconnect, [100], [111]) are shown in Fig. 22.18.

The dependence of interconnect resistance on the number of effective bonds ($R_{\mathrm{interconnect}} \times N_{eff.bonds}$) is the constant value. In the case of CNT-Au interconnect ([100]) it equals approximately 4,000 kOhm. The presented results of interconnect resistance simulations are useful, in order to consider a parametric analysis of SWCNT effective conducting channels with arbitrary chirality [46].

22.5   Conclusions

Using the *'effective bonds'* model, we have predicted the resistivity of interconnects between the metal substrate and SW or MW CNTs (SL GNR or ML GNR). There also exists a qualitative compatibility of results obtained for CNT-Me junctions using both approaches considered in this research: (i) AB-INITIO *'liquid metal'* model and (ii) semi-empirical *'effective bonds'* model based on the Landauer relationship. At the same time, the latter results are quantitatively comparable with those measured experimentally, *i.e.*, within the range of several up to 50 kOhm [44].

We have also developed the model of inter-shell interaction for MW CNTs, which allows us to estimate the transparency coefficient as an indicator of possible 'radial current' losses.

We have underscored that conductance and other current-voltaic parameters depend on the morphology of the nearest shells in MWCNTs and MLGNRs, which leads to complications for technology and production of nanodevices with stable electric characteristics.

We are able now to create a database of CNT-Metal and GNR-Metal Junctions combinations taking into account a set of parameters, and namely, the angle of chirality, the CNT diameter, the number of walls or layers, the type of metal substrate (Me), the orientation of metal substrate (e.g.(100), (111) or (110)). Thus, we are able to forecast interconnect properties for various SW-, MW CNT, SL- and MLGNR configurations.

Potential nanosensor devices on the basis of CNT, GNR and their interconnects are possible and can be very effective for external influences of various nature. They can change the electron transport regime and promote the current losses. At the same time, the interconnect interfaces can be also sensitive to chemical adsorbents, electrical and magnetic fields, changing the properties of interconnect potential barrier and efficiency of conducting channels. Both these mechanisms of nanosensing are possible to simulate in the framework of the proposed models.

References

1. Ahlskog M, Laurent C, Baxendale M, Huhtala M (2004) Electronic properties and applications of carbon nanotubes. In: Nalwa HS (ed) Encyclopedia of nanoscience and nanotechnology, vol 3. California: American Science Publishers, Stevenson Ranch, pp 139–161

2. Dresselhaus MS, Dresselhaus G, Eklund PC (1996) Science of fullerenes and carbon nanotubes. Academic, San Diego

3. Tans SJ, Verschueren RM, Dekker C (1998) Room-temperature transistor based on a single carbon nanotube. Nature 393:49–52

4. Tersoff J (1999) Contact resistance of carbon nanotubes. Appl Phys Lett 74:2122–2124

5. Shunin Yu N, Zhukovskii Yu F, Burlutskaya NY, Bellucci S (2011) Resistance simulations for junctions of SW and MW carbon nanotubes with various metal substrates. Cent Eur J Phys 9 (2):519–529

6. Wu J, Zang J, Larade B, Guo H, Xong XG, Liu F (2004) Computational designing of carbon nanotube electromechanical pressure sensors. Phys Rev B 69:153406–153409

7. Sotiropoulou S, Chaniotakis NA (2003) Carbon nanotube array-based biosensor. Anal Bioanal Chem 375:103–105

8. Ghosh S, Sood AK, Kumar N (2003) Carbon nanotube flow sensors. Science 299:1042–1044

9. Akyildiz IF, Jornet JM (2010) Electromagnetic wireless nanosensor networks. Nano Commun Netw J (Elsevier) 1(1):3–19

10. Dong L, Jiao J, Foxley S, Tuggle DW, Mosher CL, Grathoff GH (2002) Effects of hydrogen on the formation of aligned carbon nanotubes by chemical vapor deposition. J Nanosci Nanotechnol 2(2):155–160

11. Lambin P, Vigneron JP, Fonseca A, Nagy JB, Lucas AA (1996) Atomic structure and electronic properties of a bent carbon nanotube. Synth Met 77:249–252

12. Chico L, Crespi VH, Benedict LX, Louie SG, Cohen ML (1996) Pure carbon nanoscale devices: nanotube heterojunctions. Phys Rev Lett 76:971–974

13. Rochefort A, Salahub DR, Avouris P (1998) The effect of structural distortions on the electronic structure of carbon nanotubes. Chem Phys Lett 297:45–50

14. Zhao B, Itkis ME, Niyogi S, Hu H, Perea DE, Haddon RC (2004) Extinction coefficients and purity of single-walled carbon nanotubes. J Nanosci Nanotechnol 4:995–1004

15. Wong EW, Sheehan PE, Lieber CM (1997) Nanobeam mechanics: elasticity, strength, and toughness of nanorods and nanotubes. Science 277:1971–1975

16. Paladugu MC, Maneesh K, Nair PK, Haridoss P (2005) Synthesis of carbon nanotubes by arc discharge in open air. J Nanosci Nanotechnol 5:747–752

17. Rochefort A, Avouris P, Lesage F, Salahub DR (1999) Electrical and mechanical properties of distorted carbon nanotubes. Phys Rev B 60:13824–13830

18. Gajewski S, Maneck HE, Knoll U, Neubert D, Dorfel I, Mach R, Strauss B, Friedrich JF (2003) Purification of single walled carbon nanotubes by thermal gas phase oxidation. Diamond Relat Mater 12:816–820

19. Joseph H, Swafford B, Terry S (1997) MEMS in the medical world. Sens Mag 14:47–51

20. Hsu TR (2002) MEMS and microsystems: design and manufacture. McGraw-Hill, Boston

21. Ivnitski D, Abdel-Hamid I, Atanasov P, Wilkins E, Stricker S (2000) Application of electro-chemical biosensors for detection of food pathogenic bacteria. Electroanalysis 12:317–325

22. Chopra S, McGuire K, Gothard N, Rao AM (2003) Selective gas detection using a carbon nanotube sensor. Appl Phys Lett 83:2280–2282

23. Ong KG, Zeng K, Grimes CA (2002) A wireless, passive carbon nanotube-basedgas sensor. IEEE Sens J 2:82–88

24. Wong YM, Kang WP, Davidson JL, Wisitsora-at A, Soh KL (2003) A novel microelectronic gas sensor utilizing carbon nanotubes for hydrogen gas detection. Sens Actuators B 93:327–332

25. Cinke M, Li J, Chen B, Cassell A, Delzeit L, Han J, Meyyappan M (2002) Pore structure of raw and purified HiPco single-walled carbon nanotubes. Chem Phys Lett 365:69–74

26. Desai SC, Willitsford AH, Sumanasekera GU, Yu M, Tian WQ, Jayanthi CS, Wu SY (2010) Hypergolic fuel detection using individual single walled carbon nanotube networks. J Appl Phys 107:114509–114516

27. Shunin Yu N, Schwartz KK (1997) Correlation between electronic structure and atomic configurations in disordered solids. In: Tennyson RC, Kiv AE (eds) Computer modelling of electronic and atomic processes in solids. Kluwer Academic. Publisher, Dodrecht/Boston/London, pp 241–257

28. Shunin Yu N, Zhukovskii Yu F, Bellucci S (2008) Simulations of properties of carbon nanotubes using the effective media approach. Comput Model New Technol 12(2):66–77

29. Ziman JM (1979) Models of disorder. Cambridge University Press, New York, Chap. 10

30. Shunin Yu N (1991) Simulation of atomic and electronic structures of disordered semiconductors, Dr.Sc.Habil. Thesis (Phys.& Math.). Riga-Salaspils

31. Gaspar R (1952) Über ein analitisches Näharungsverfachren zur Bestimung von Eigenfunktionen und Energieeigenwerten von Atomelektronen. Acta Phys Acad Sci Hung 2:151–178; Über eine Approximation des Hartree-Fockschen Potential dürch eine universelle Potentialfunktion. Acta Phys Acad Sci Hung 3:263–286

32. Economou EL (2006) Green's functions in quantum physics, vol 7, 3rd edn, Solid State Ser. Springer, Berlin/Heidelberg

33. Slater JC (1974) The self-consistent field for molecules and solids, vol 4. McGraw-Hill Book Company, New York

34. Ehrenreich H, Schwartz L (1976) The electronic structure of alloys. In: Solid state physics, vol 31. Academic Press, New York/San Francisco/London

35. Soven P (1967) Coherent-potential model of substitutional disordered alloys. Phys Rev 156:809–813

36. Stone D, Szafer A (1988) What is measured when you measure a resistance? The Landauer formula revisited. IBM J Res Dev 32(3):384–413

37. Ding F, Larsson P, Larsson JA, Ahuja R, Duan H, Rose A, Bolton K (2008) The importance of strong carbon-metal adhesion for catalytic nucleation of single-walled carbo nanotubes. Nano Lett 8:463–468

38. Shunin Yu N (2009) Generic challenges for fundamental research in Nanomaterials science. In: Dosch H, Van de Voorde MH (eds) GENNESYS white paper. Max-Planck-Institut für Metallforschung, Stuttgart, pp 8–29

39. Uryu S (2004) Electronic states and quantum transport in double-wall carbon nanotubes. Phys Rev B 69:075402–075412

40. Lunde AM, Flensberg K, Jauho A-P (2005) Intershell resistance in multiwall carbon nanotubes: a Coulomb drag study. Phys Rev B 71:125408–125425

41. Kordrostami Z, Sheikhi MH, Mohammadzadegan R (2008) Modeling electronic properties of multiwall carbon nanotubes. Fuller Nanotub Carbon Nanostruct 16(1):66–77

42. Shunin Yu N, Zhukovskii Yu F, Burlutskaya N, Gopeyenko VI, Bellucci S (2010) Theoretical resistance simulations for junctions of SW and MW carbon nanotubes with metal substrates in nanoelectronic devices. Comput Model New Technol 14(2):7–19

43. Shunin Yu N, Zhukovskii Yu F, Gopejenko VI, Burlutskaya N, Bellucci S (2011) *Ab Initio* simulations on electric properties for junctions between carbon nanotubes and metal electrodes. Nanosci Nanotechnol Lett 3:816–825

44. Jeong-O Lee, Park C, Ju-Jin Kim, Jinhee Kim, Jong Wan Park, Kyung-Hwa Yoo (2000) Formation of low-resistance ohmic contacts between carbon nanotube and metal electrodes by a rapid thermal annealing method. J Phys D Appl Phys 33:1953–1956

45. Shuba MV, Slepyan GYa, Maksimenko SA, Thomsen C, Lakhtakia A (2009) Theory of multiwall carbon nanotubes as waveguides and antennas in the infrared and the visible regimes. Phys Rev B 79:155403–155420

46. Miano G, Forestiere C, Maffucci A, Maksimenko SA, Slepyan GY (2011) Signal propagation in carbon nanotubes of arbitrary chirality. IEEE Trans Nanotechnol 10(1):135–149